stellarator news

Published by Fusion Energy Division, Oak Ridge National Laboratory
Building 9201-2 P.O. Box 2009 Oak Ridge, TN 37831-8071, USA

Editor: James A. Rome Issue 84 November 2002
E-Mail: jar@ornl.gov Phone (865) 574-1306
On the Web at *http://www.ornl.gov/fed/stelnews*

Observation of poloidal rotation in the Uragan-3M torsatron using edge H_α fluctuation correlation studies

Introduction

Poloidal plasma rotation induced by $\mathbf{E} \times \mathbf{B}$ drift is one of the most popular topics of toroidal magnetic plasma confinement experiments. The most direct means of observing poloidal rotation is by measuring the Doppler shift of spectral lines of impurity ions emitted in a corresponding direction [1]. Spatial resolution of the measurements is provided by using atomic beams (diagnostic or heating ones) crossing a plasma column. In this case the velocity of charge-exchanged impurity ions is measured and yields information about the poloidal rotation of these ions. This velocity does not necessarily coincide with the velocity of main (hydrogen) plasma ions.

Recently microwave reflectometry has become popular for observation of poloidal plasma rotation [2,3]. This technique is based on observation of microwaves reflected by plasma cut-off layers perturbed by plasma fluctuations. Such layers act like a diffraction grating that is moving across the observation line and causes reflected microwave modulation. Information about this movement can be inferred from observation of the Doppler-shifted spectrum of reflected microwaves at oblique reflection [2] or from cross-correlation of microwaves reflected from two different poloidal locations [3]. In this approach the observed frequency shift or time delay is a result of the propagation of electron density perturbations and is influenced by fluctuation poloidal propagation and by plasma column rotation (if it occurs).

In this work we tried to deduce the propagation of electron density perturbations at the plasma edge from observations of H_α plasma emission. This approach is based on the fact that the H_α line intensity in a plasma with an electron temperature ≥ 5–10 eV depends only on the hydrogen atom and electron density. In a fluctuating plasma, H_α light fluctuations are mostly the result of fluctuations in electron density n_e, thus making it possible to study n_e fluctuations.

Experiment

Experiments were performed during radio-frequency (rf) plasma production/heating on the torsatron Uragan-3M (U-3M) [4]. Figure 1 shows a cross section of the $l = 3$ helical winding (one winding is not shown) and magnetic surfaces for the standard U-3M magnetic field configuration. H_α light emission was observed through a window by means of a simple two-channel lens/H_α filter/photomultiplier (PMT) system. Each system could scan the whole plasma cross section.

In this issue . . .

Signals from PMT were digitized (sampling rate up to 1.5 million 12-bit words/s), stored, and analyzed.

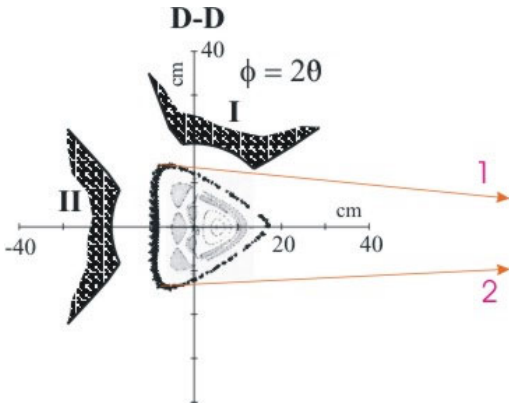

Fig. 1. Schematic view of the experiment. The observation lines are labeled 1 and 2.

A typical H_α signal for the experiment (B = 0.7 T, P_{rf} = 200 kW) is shown in Fig. 2 with the signal from the 2-mm interferometer. Shot-to-shot scanning of the observation lines for both channels (Fig. 3) allowed selecting positions of the channels to observe light from opposite lobes of the magnetic surfaces.

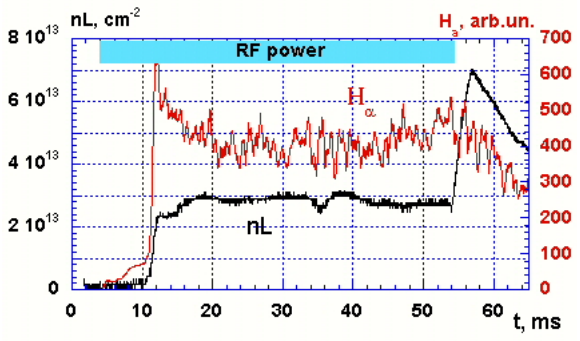

Fig. 2. Typical signals of H_α and 2-mm interferometer (sampling rate: 200,000 samples per second).

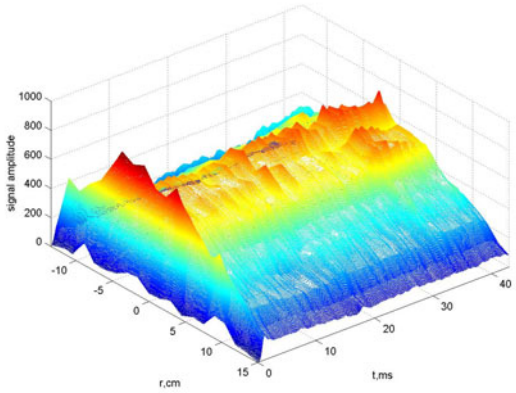

Fig. 3. Contour plot of side-on observation of H_α emission.

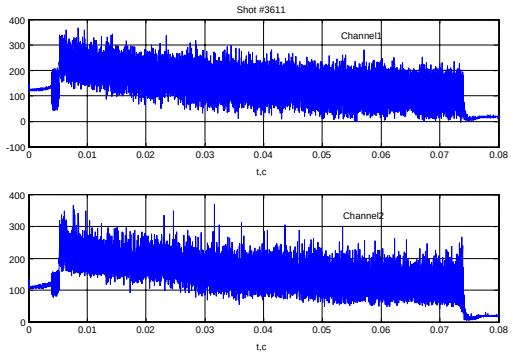

Fig. 4. H_α signals for both channels (sampling rate: 1 million samples per second).

Analysis of fluctuations included calculation of the power spectrum of H_α signals, cross-correlation functions $C_{12}(\tau)$ and coherence functions $C_{12}(\omega)$ of 1024 data points extracted from the signals (sampling rate: 1 Ms/s). Figure 4 shows typical signals from both channels with a higher sampling rate.

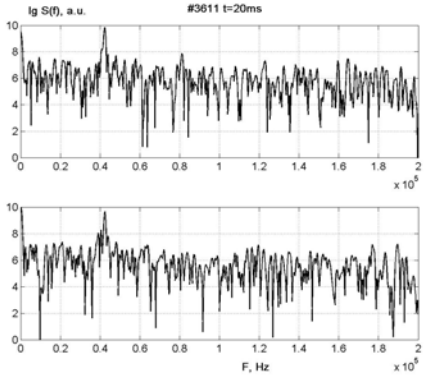

Fig. 5. Spectra of signals of both channels. The *y*-axis is a logarithmic scale.

Typical spectra of the H_α light fluctuations are shown in Fig. 5. These spectra are characterized by a slow fall-off with frequency and do not depend on time for the period from 20 to 50 ms. Cross-correlation between the signals for the same time window is shown in Fig. 6.

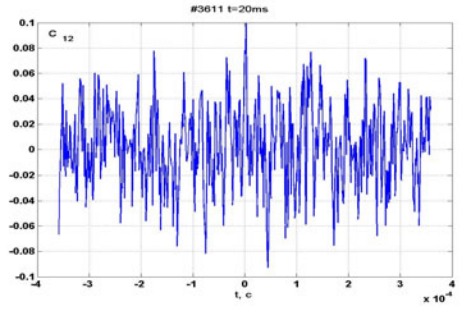

Fig. 6. Cross-correlation between the signals from the two channels.

The most striking feature of cross-correlation between the H_α signals from different poloidal locations is a maximum at zero lag time. This means that the observed fluctuations must be due to poloidal propagation that manifests itself in observed fluctuations (possibly a ballooning mode). Poloidal propagation of density perturbations can be responsible for other maxima of $C_{12}(\tau)$.

To get more information about poloidal propagation of perturbations, we used another approach: filtering of rather narrow frequency bands (δf = 2–3 kHz) of signal and calculation of the time lag between these filtered signals. For this approach we used a numerical double filtering procedure that eliminates the phase delay produced by signal filtering. Typical cross-correlation for filtered signals is shown in Fig. 7.

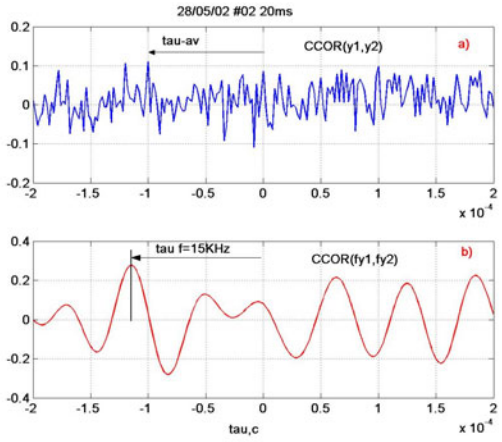

Fig. 7. Cross-correlation for (a) non-filtered, and (b) filtered signals (f = 15 kHz).

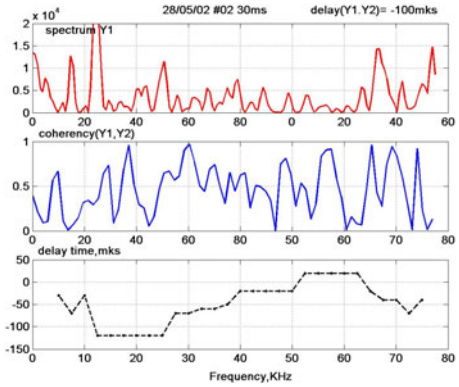

Fig. 8. Power spectrum, coherency function, and time lag spectrum of H_α light fluctuations for t = 20 ms.

Results of calculations of time lag for filtered signals and their dependence on filter frequency, together with the power spectrum and coherency function, are shown on Fig. 8.

Analysis of data for different shots, and time intervals for a given shot, allowed us to distinguish for different frequency bands: (1) a low-frequency band (12–25 kHz) with almost constant delay time ($\delta t = -120$ μs); (2)an intermediate frequency band (25–50 kHz) with changing delay time; and (3) a high-frequency band (52–60 kHz) with small delay time ($\delta t = 20$ μs). Because the delay time in the first band roughly coincides with one of the maxima in the cross-correlation for unfiltered signals, we suggest that poloidal plasma rotation is responsible for this delay time. Also, the small delay time in band 3 might reflect the existence of a zero lag time maximum in the cross-correlation for the unfiltered signal and thus correspond to a ballooning mode of the perturbations. We also suggest that band 2, with a changing delay time, reflects the existence of perturbations propagating in the poloidal direction. Data for delay time in this band were used for calculation of a velocity of propagation v and a dispersion relation for this frequency band

$$\omega = k \cdot v .$$

Figure 9 illustrates results of these calculations (points). For poloidal modes one can suggest that

$$k = m/a , \qquad (1)$$

where m is the mode number (1, 2, ...) and a is the plasma layer radius ($a \sim 12$ cm). Horizontal lines on Fig. 9 show k-values calculated from Eq. (1). Mode frequencies (intersections of the dotted line and horizontal bars) roughly coincide with the spectrum and coherence function maxima in band 2.

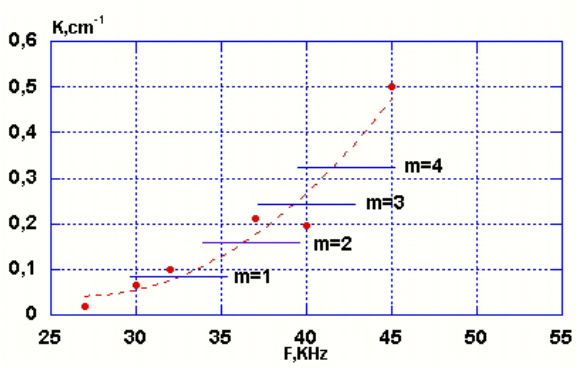

Fig. 9. k_θ spectrum for f = 27–45 kHz.

Conclusion

Studies of the properties of fluctuations of H_α light emitted from the edge plasma in the U-3M torsatron showed a rather complicated picture in which the effects of possible poloidal plasma rotation could not be distinguished through analysis of cross-correlation data. We introduced a new function, the time lag spectrum $\tau_{12}(f)$, and calculated it by using digital filtering of H_α signals. This function appears to give information about different modes of perturbations — poloidally propagating and ballooning modes and poloidal plasma rotation. Such an approach can be used for fluctuations observed by any diagnostic if it has good spatial and time resolution and has at least teo spatially-separated observation channels.

The poloidal rotation velocity inferred from the time delay of the low-frequency part of the H_α fluctuation spectrum (v_{pol} = 3 km/s) agreed well with data obtained for the U-3M torsatron via poloidal correlation microwave reflectometry [4].

The main disadvantage of using H_α light — the lack of good spatial distribution — can be overcome by beam-emission spectroscopy (BES) if diagnostic or heating neutral beams are available.

A similar setup for H_α observation is now under preparation for the Compact Helical System (CHS) Heliotron/torsatron.

References

[1] G. R. McKee, M. Murakami et al., Plasma Phys. **7** (2000) 1870.

[2] V. V. Bulanin, S. V. Lebedev et al., Plasma Phys. Rep. **26** (2000) 823.

[3] [A. I. Skibenko, V. L. Ocheretenko et al., Ukrainian Journ. of Phys., **46** (2001) 443.

[4] A. I. Skibenko, O. S. Pavlichenko et al., "ITB formation dynamics in the U-3M torsatron inferred from microwave reflectometry," p 52 in Abstracts: *Int. Conf. School on Plasma Physics and Controlled Fusion, Alushta, 2002* (proceedings to be published in Vopr. Atom.Nauk. Tekh.).

O. S. Pavlichenko,[1] V. G. Konovalov,[1] K. Matsuoka,[2] A.N. Shapoval,[1] A. I. Skibenko,[1] C. Suzuki[2]

E-mail: pavlich@ipp.kharkov.ua

[1] Institute of Plasma Physics,
NSC Kharkov Institute of Physics and Technology
Kharkov, Ukraine

[2] National Institute for Fusion Studies, Toki, Japan

Integrated plasma and coil optimization for compact stellarators

Compact stellarators are toroidal confinement devices with low aspect ratio $2 < A < 5$ ($A = \langle R \rangle / \langle a \rangle$), a small number of toroidal field periods ($2 \le N_p \le 4$), and bootstrap current producing a small fraction of the magnetic rotational transform. They have been developed to combine the advantages of stellarators (in particular, steady-state operation and the avoidance of disruptions) and tokamaks (e.g., good particle and energy confinement at high beta) in an efficient and cost-effective plasma configuration. Examples are the National Compact Stellarator Experiment (NCSX), a proof-of-principle compact stellarator with $A = 4.4$ and $N_p = 3$, and the $A = 2.7$, $N_p = 2$ Quasi-Poloidal Stellarator (QPS), a concept exploration device.

The stellarator optimization code STELLOPT [1] has been used in recent NCSX and QPS design studies to determine the shape of the outer magnetic flux surface, and the internal plasma pressure and current profiles, that approximate a prescribed rotational transform, limit particle drift trajectories, and lead to attractive plasma stability and confinement properties at significant beta. Some coil-related figures of merit (e.g., measures of coil complexity, curvature, and current density) are included in the optimization, using the NESCOIL [2] model, in order to guide the plasma configuration toward a region in parameter space that can be accessed in the subsequent coil design. In a separate step in the design process, the coil optimization code COILOPT [3] solves for the coil geometry and current distribution that will best approximate the physics solution in a free-boundary MHD equilibrium calculation. Both are computationally intensive optimization problems, and even after several iterations of the two-step process, it is often difficult to produce a coil design that meets practical engineering design standards.

We describe the results of a new method that includes both the plasma and coil models in a combined optimization to ensure that physics and engineering goals are simultaneously satisfied. The self-consistent analysis is successful largely because it is implemented only after the separate optimization studies have identified a good candidate for the design point, thus providing an initial "guess" for the local minimization that includes both plasma and coil models.

Integrated optimization of plasma and coils

The compact stellarator coil system, consisting of modular coils to provide the helical field, and toroidal field (TF) coils and vertical field (VF) coils for configuration flexibility, is designed to minimize the normal component of the magnetic field (which may include a component due to a net plasma current [4]) relative to a reference plasma surface. The coils are subject to engineering constraints such as minimum coil separation and minimum radius of curvature. The reference plasma shape is the result of a separate optimization targeting plasma stability and confinement at reference values of beta, consistent with a fixed-boundary MHD equilibrium obtained using VMEC [5]. A solution to the coil design problem is a feasible point with respect to engineering constraints that will accurately reconstruct the reference plasma boundary shape in a free-boundary VMEC MHD equilibrium calculation where, given the same plasma current and pressure profiles, the plasma shape is self-consistent with the external field due to the coils.

In the STELLOPT code, the stellarator design optimization problem is formulated as a least-squares problem to minimize $\chi^2 = \sum \chi_i(\mathbf{x})^2$, where the components χ_i are (generally nonlinear) functions of the system parameters **x**. The independent variables **x** include coefficients describing the MHD plasma equilibrium pressure and current profiles, as well as (1) Fourier coefficients of the plasma shape, in the case of a fixed-boundary optimization, or (2) coil currents, if the optimization is to be executed in free-boundary mode. The functions χ_i are stellarator physics figures of merit and engineering con-

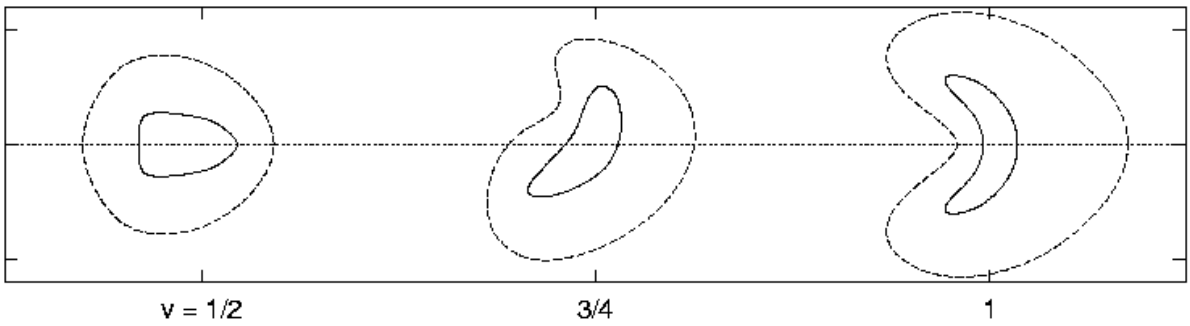

Fig. 1. The optimized coil-winding surface shape (dashed line) and reference plasma shape (solid line) shown for three planes in the normalized toroidal angle (v).

straints, which are evaluated numerically using a set of complex plasma physics and engineering models that depend on the solution of a three-dimensional (3D) plasma MHD equilibrium. STELLOPT uses the Levenberg-Marquardt (LM) method to solve the nonlinear least-squares problem. Subroutines interface each physics and engineering model with the optimization code, and several models (e.g., NEO [6], COBRA [7], NESCOIL) are evaluated as executables through system calls from these subroutines.

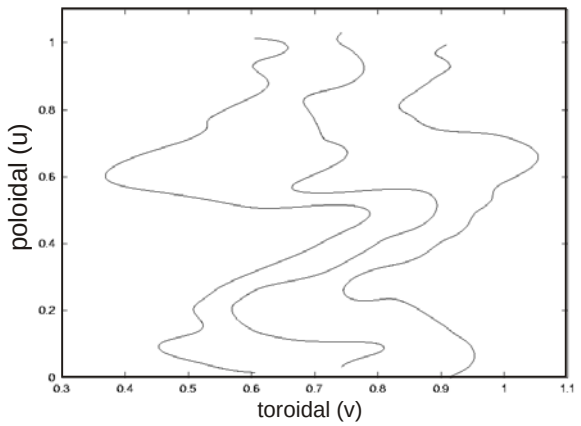

Fig. 2. The NCSX modular coils consist of three distinct coil types, shown as a function of the normalized toroidal (v) and poloidal (u) angles.

The COILOPT code is based on a parametric representation of stellarator coils confined to a coil-winding surface (CWS), as shown in Fig. 1. The winding law (Fig. 2) for modular coils on this surface is given either by Fourier series or by a cubic spline representation. The winding law coefficients, CWS coefficients, and the coil currents are all possible independent variables in the coil optimization problem. COILOPT also uses the LM method to solve the nonlinear optimization. Components of the objective function include residuals in the normal component of the magnetic field on the targeted plasma surface, together with engineering constraints on coil geometry.

In the integrated plasma/coil optimization, the elements of the vector $\mathbf{x}$ consisting of Fourier coefficients of the plasma boundary in the STELLOPT calculation are replaced by the independent variables of the coil optimization problem. In addition, COILOPT is executed from STELLOPT in a mode where only the functions $\chi_i(\mathbf{x})$ for coil geometry constraints are evaluated. Here VMEC is executed in the free-boundary mode. A consistent solution is achieved by targeting the physics parameters of the reference plasma and the geometric properties necessary for engineering coil design, while allowing the plasma boundary shape to vary from the original reference.

Configuration Optimization of the NCSX

The goals of the NCSX are to explore the physics of 3D plasma shaping at high beta with rotational transform due to both internal and external currents and to study the effect of quasi-axisymmetry on plasma confinement. The NCSX is a proof-of-principle device with average major radius $\langle R \rangle$ = 1.4 m, magnetic field $\langle B \rangle$ = 1.7 T, and

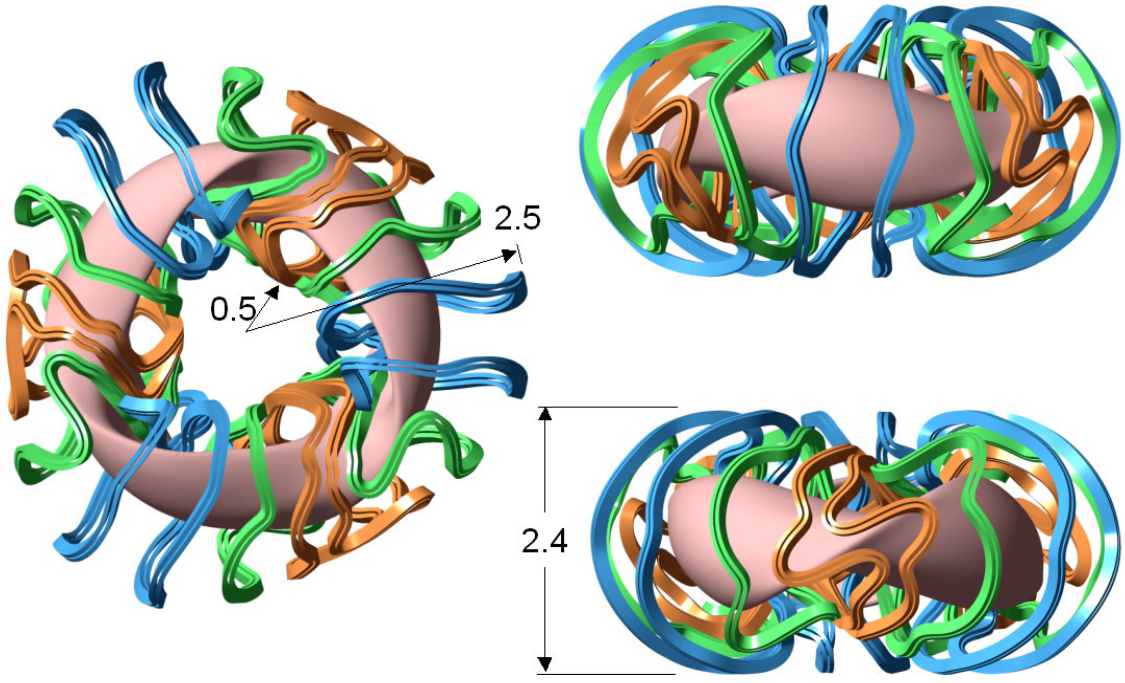

Fig. 3. NCSX plasma and modular coils.

$\langle\beta\rangle$ = 4%. The NCSX magnetic coil design consists of 18 modular coils (3 coil types, Fig. 3) and 18 TF coils, six pairs of poloidal field (PF) coils, and trim coils. In addition to the usual coil geometry constraints, the NCSX coil design targets include constraints on the winding surface, imposed by an internal vacuum vessel, and access requirements for neutral beam injection (NBI). Coil optimization studies have considered (1) the number of modular coils per field period, (2) the position of the coils relative to the plasma symmetry planes, and (3) the role of TF and PF coils in the modular coil optimization and plasma flexibility analysis. Representative configurations from the sequence of numerical optimizations leading to design M45 for NCSX are summarized in Table 1. The LI383 plasma configuration was the result of an extensive set of fixed-boundary STELLOPT calculations, and provided an initial target for COILOPT investigations. Experience showed that obtaining levels of confinement and stability comparable to the LI383 target required an approximation of the normal magnetic field at the plasma boundary ∂P in the coil optimization with an average error

$$\langle \delta B \rangle = (1/A) \int_{\partial P} \frac{|\mathbf{B} \cdot \mathbf{n}|}{|\mathbf{B}|} dA \leq 6\% .$$

COILOPT was used to find coil designs with 21 modular coils (M12) and ith 18 modular coils (M25) that adequately reconstructed the plasma properties of LI383 in free-boundary STELLOPT studies, including, e.g., marginally stable beta (for $\langle\beta\rangle$ = 4%), effective ripple factor ($\varepsilon_{eff}^{3/2}$), and neutral beam energy loss fraction (f_{NB}). These designs, however, did not fully meet engineering feasibility requirements. It was not until the coil engineering targets in COILOPT were combined with the plasma optimization in STELLOPT that a family of consistent solutions M45 (Fig. 3) was found. The LI383 plasma configuration and the M25 coils provided a starting point for the M45 combined optimization. The final step in the NCSX physics design was to make corrections in the modular coil geometry to reduce the width of targeted magnetic islands. Hudson et al. describe an algorithm [8] using the PIES code [9] to make small adjustments in the modular coils, also subject to COILOPT constraints on coil geometry, in order to recover good magnetic surface quality.

Table 1. Design optimization of the NCSX

Configuration	LI383	M12	M25	M45
A	4.36	4.36	4.34	4.37
$\langle\beta\rangle$ (%)	4.19	4.09	4.05	4.08
$\varepsilon_{eff}^{3/2}$ ($\times 10^4$), center	0.24	0.32	0.41	0.96
f_{NB} (%)	14.5	14.2	13.5	15.5
Δ_{min}, coil-coil (cm)		12.8	11.9	16
Δ_{min}, coil-plasma (cm)		17.5	19.9	18.7
Δ_{min}, NBI access (cm)			30.9	37.4
Minimum bend radius (cm)		7.7	9.4	10.5

Design optimization of the QPS

A parallel effort used the STELLOPT, COILOPT, and merged optimization codes to design the QPS, a concept exploration device to investigate the effects of 3D shaping and quasi-poloidal symmetry ($(\partial|\mathbf{B}|)/(\partial\theta) \approx 0$, where θ is a poloidal angle) on neoclassical confinement at moderate beta. The QPS plasma has N_p = 2, A = 2.7, $\langle R\rangle$ = 0.9 m, magnetic field B = 1 T, and target $\langle\beta\rangle$ = 1.8%. The QPS coil design (Fig. 4) consists of 16 modular coils (4 coil types, where the winding packs of the pair of coils near the center of the long section in Fig. 4 follow independent paths), 12 TF coils, and 2 pairs of circular VF coils. In addition to the usual coil engineering constraints, modular coil optimization targets QPS-specific constraints, such as space in the center of the device for the TF coil legs and solenoid coils.

Results are summarized in Table 2. On the basis of confinement properties significantly better than those of the original GB4 solution, as well as plasma flexibility considerations (e.g., vacuum field properties), configuration 0411 was chosen as an initial design point for an integrated plasma and coil optimization with STELLOPT to produce the QPS reference configuration 0718. Configuration 0411 was a result of the separate plasma and coil design optimizations and provided an adequate reconstruction of the targeted fixed-boundary plasma shape and plasma properties. While coil geometry metrics were also acceptable, the coil design required a large number of winding law coefficients (28) and CWS modes (41), resulting in a very complex winding surface shape. In this case, the merged optimization was an attempt to obtain a solution with comparable plasma properties using a smaller number of free parameters in the coil winding law and CWS (leading to less complex coil manufacturing properties), while allowing the equilibrium plasma shape to change in a self-consistent manner. Solution 0718

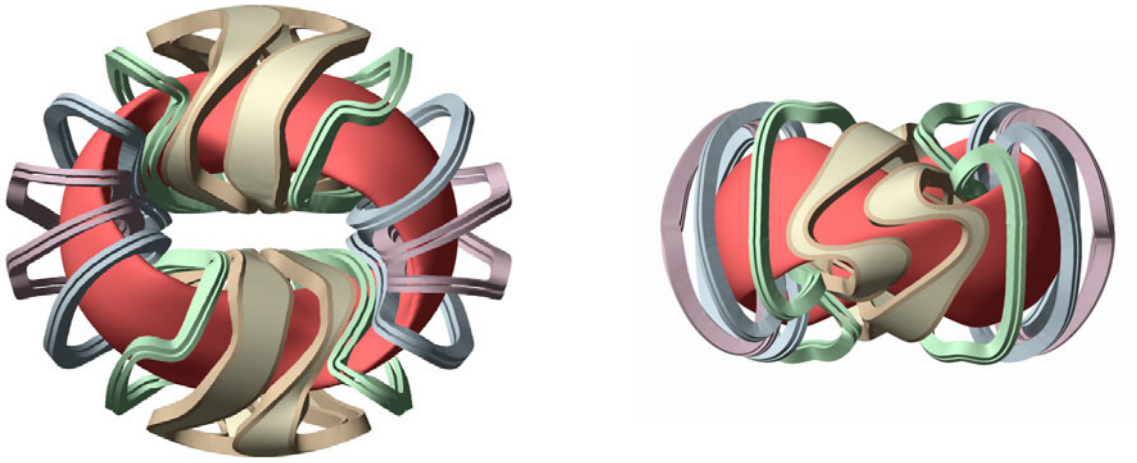

Fig. 4. QPS plasma boundary and modular coils for configuration 0718.

achieved this goal with 15 coil winding law coefficients, and 23 CWS coefficients.

Table 2. Design optimization of QPS

Configuration	GB4	411	718
A	2.62	2.71	2.67
$\langle\beta\rangle$ (%)	1.88	1.78	1.83
$\varepsilon_{\rm eff}^{3/2}$ ($\times 10^3$), center	33.1	4.3	2.4
ι (axis)	0.27	0.29	0.28
ι (edge)	0.4	0.38	0.34
$\Delta_{\rm min}$, coil-coil (cm)	11.4	10.1	9.6
$\Delta_{\rm min}$, coil-plasma (cm)	13.4	14.6	13
Minimum bend radius (cm)	7.2	10.1	9.3

References

[1] D. A. Spong et al., Nucl. Fusion **41** (2001) 711.

[2] P. Merkel, Nucl. Fusion **27** (1987) 867.

[3] D. J. Strickler et al., Fusion Sci. Technol., **41** (2002) 107.

[4] P. Merkel and M. Drevlak, in Proc. Int. Congress Plasma Physics (ICPP 98) and 25th Conf. Controlled Fusion Plasma Physics, Prague, Czech Republic, June 29–July 3, 1998, ECA Vol. 22C, pp. 1745–1748 (1998).

[5] S. P. Hirshman and J. C. Whitson, Phys. Fluids **26,** 3553 (1983) 12.

[6] V. V. Nemov et al., Phys. Plasmas **6** (1999) 4622.

[7] R. Sanchez et al., J. Comput. Phys. **161** (2000) 576.

[8] S. R. Hudson et al., Plasma Phys. and Controlled Fusion **44** (2002) 1377.

[9] A. H. Reiman et al., Phys. Plasmas **8** (2001) 2083.

D. J. Strickler, L. A. Berry, S. P. Hirshman, J. F. Lyon,
D. A. Spong, D. E. Williamson
Oak Ridge National Laboratory

M. C. Zarnstorff, L-P. Ku, A. Brooks, S. R. Hudson,
D. A. Monticello, G. H. Neilson,
N. Pomphrey, A. H. Reiman
Princeton Plasma Physics Laboratory

A. S. Ware
University of Montana–Missoula

E-mail contact: stricklerdj@ornl.gov

Research supported by the U.S. Department of Energy under Contract DE-AC05-00OR22725 with UT-Battelle, LLC, Contract DE-AC76-CH0-3073 with the Princeton Plasma Physics Laboratory, and Grant DE-FG03-97ER54423 at the University of Montana.